Available online at www.sciencedirect.com

ScienceDirect

materialstoday: PROCEEDINGS

Materials Today: Proceedings 2S (2015) S511 – S516

International Conference on Martensitic Transformations, ICOMAT-2014

Superelastic Nickel-free porous materials for load-bearing medical implants: Fabrication and modeling

V. Brailovski[a,]*, P. Terriault[a], S. Prokoshkin[b], C. Simoneau[a], J. Rivard[a], S. Dubinskiy[b]

[a]*Ecole de technologie supérieure, 1100 Notre-Dame Street West, Montreal (Quebec) H3C 1K3, Canada*
[b]*National University of Science and Technology "MISiS", Leninskii pr.4, Moscow, Russia*

Abstract

The objective of this work is to create a new class of porous metallic implant materials combining the biocompatibility of pure titanium with the superelasticity of Nitinol. Ti-20.8Nb-5.5Zr, Ti-22Nb-6Ta (at%) and Ti-CP foams are produced by the space-holder technique and characterized from both the pore morphology and the mechanical behavior points of view. To support these developments, a multi-scale representative volume element-based approach is proposed and experimentally validated. Using this approach, the implant's porosity can be engineered, and the base material properties adjusted, so that the implant could offer adequate pore morphology for bone ingrowth while offering high mechanical resistance.

Selection and Peer-review under responsibility of the chairs of the International Conference on Martensitic Transformations 2014.

Keywords: nickel-free shape memory alloys; metallic foams, medical implants, space-holder technique, representative volume element

1. Introduction

It has been clearly demonstrated that the long-term clinical performances of metallic implants are improved significantly when they possess an open-cell porous structure, thereby reducing stiffness mismatch and allowing stable fixation by means of bone ingrowth [1,2]. Furthermore, this structure allows the implant to be lighter than an equivalent solid structure while maintaining mechanical integrity. It has also been proven that porous superelastic

* Corresponding author. Tel.: 1-514-396-8594; fax: 1-514-396-8530.
E-mail address: vladimir.brailovski@etsmtl.ca

Selection and Peer-review under responsibility of the chairs of the International Conference on Martensitic Transformations 2014.
doi:10.1016/j.matpr.2015.07.337

implants made of Ti-Ni outperform porous implants made of pure titanium in terms of bone ingrowth under load-bearing in vivo conditions, due to their enhanced biomechanical compatibility [3]. The positive outcome of this last study makes it possible to suggest that porous superelastic implants made of Ni-free titanium alloys [4,5] should result in even higher long-term clinical performance than their Ti-Ni counterparts, as they contain only highly compatible components.

Generally speaking, the functional requirements for porous scaffolds can be divided into two groups: structural (pore size, distribution and interconnectivity) and mechanical (stiffness, mechanical resistance and elastic strain). The implant's porosity should be engineered so that it offers a compromise between maintaining the mechanical strength of the implant while providing adequate pore size for bone ingrowth, and matching the behavior of surrounding bone. The latter feature should allow ingrowing bone tissue to be mechanically strained at a beneficial level of several millistrains, preventing excessive shear displacement at the bone-implant interface, and thereby promoting new bone formation [6,7].

Different materials (such as Ta, Ti and Ti alloys) and different manufacturing techniques can be used to produce such porous structures. Among them are polymer foam-replicating technologies using either deposition or infiltration techniques, additive manufacturing powder-bed or free-form laser/electron beam melting techniques, and foaming or passive space agent power metallurgy-based techniques [8].

In this work, state-of-the-art space-holder technology is used to produce porous metallic implant materials (foams). To support these developments, a novel multi-scale representative volume element-based approach is proposed and partially validated. This communication is divided into three parts. The technological aspects of the foam's manufacturing are addressed first. Next, the principles of the multi-scale modeling of these structures are elaborated, and finally, the numerical and experimental results are compared.

2. Foam manufacturing and characterization

2.1. Manufacturing

Metallic foams were manufactured using the powder metallurgy-based space-holder technique, which has five common steps: mixing, pressing, space-holder pyrolysis, sintering and post-sintering thermal treatment. This processing sequence started with two components in powder form: a prealloyed metal powder and a spacer polymer powder. The metal powders were: commercially-pure Grade 2 titanium (TiCp), Ti-20.8Nb-5.5Zr (TNZ) and Ti-22Nb-6Ta (TNT) alloys (at%). The spacer material was polymethylmethacrylate (PMMA) powder.

The following powder granulometries (d10, d50 and d90) were used: 20, 35 and 60 μm for metallic powders and 50, 120 and 230 μm for the spacer. The mixture was uniaxially compressed (180 MPa), and the resulted green product was subjected to two-step heating to produce a brown product ($1x10^{-2}$ mbar vacuum, 2h space holder pyrolysis at 450 ^{o}C) and then a final product ($1x10^{-6}$ mbar vacuum, 3h sintering at 1300, 1400 and 1500 ^{o}C for TiCp, TNZ and TNT respectively). The details of the foam manufacturing are reported in [9]. The produced foams (Fig. 1) were then characterized from both the pore morphology and the mechanical behavior points of view.

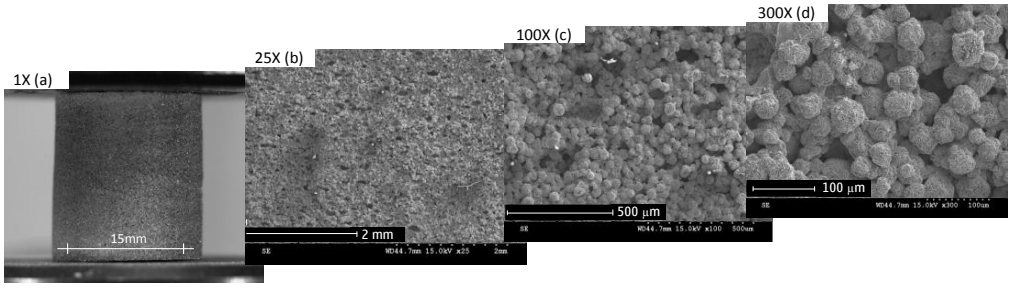

Fig. 1. Ti foam (P=0.5, P stands for porosity): photo (a), SEM images at magnifications of 25X (b), 100X (c), and 300X (d) (adapted from [9]).

2.2. Microstructure and Morphology

At room temperature, the as-sintered TNZ and TNT foams have mainly cubic β-phase structure (a = 0.33001 ± 0.00001 nm and 0.32855 ± 0.00001 nm respectively) and small quantities of α', α'' phases, and interstitial phases: TiC, (Nb,Ti)C, NbC (carbides); rutile/anatase TiO2 (oxides). The precise assessment of the α''-phase is complicated by a net overlapping of α''-phase and interstitial phases X-ray lines.

An analysis of the pore size and distribution was conducted using a combination of the image processing, mercury porosimetry and Archimedes' techniques. As an example of the image processing measurements using *ImageJ* software, Fig. 2a shows a metallographic image of the TNZ P=0.47 foam, Fig. 2b shows the binarized (black & white) image, and Fig. 2c, the pore size distribution. The calculated pore size distribution (D10, D50 and D90) for this case is 65, 250 and 870 µm. Note that for each measurement, the total number of pores analyzed varied from 9000 to 25000, depending on the foams' porosity. Interpore (pore throat) size and distribution were measured using mercury intrusion technique and it was found that the ratio of the pore size to the pore-throat size is approximately 10:1. More details on the foams morphology can be found in [9].

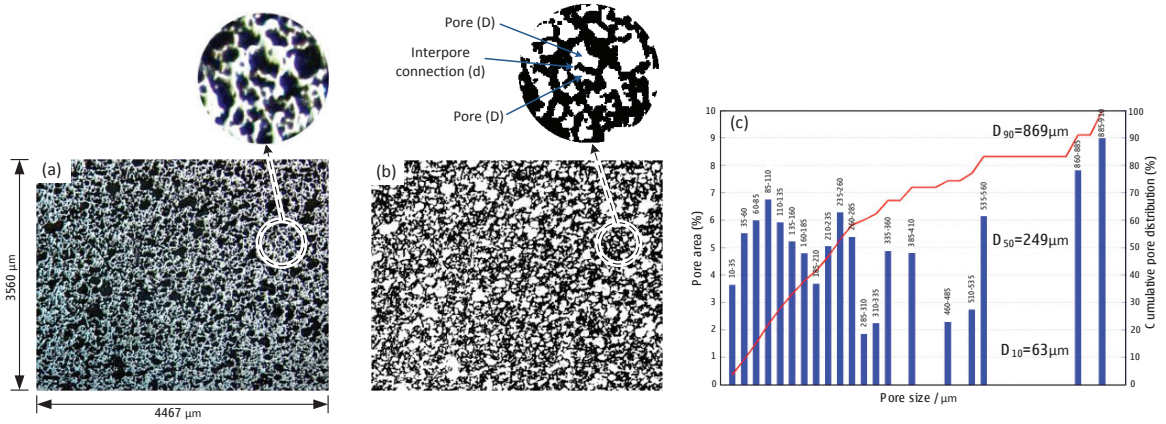

Fig. 2. TNZ foam (P=0.47): (a) metallography (25X), (b) binarized image (pores are white), and (c) pore size distribution (adapted from [9]).

2.3. Mechanical properties

Cyclic compression tests with incrementally-increased engineering strain up to ε = 0.6 or specimen failure (ε at each cycle corresponds to 0.02 of the initial sample height) were performed (ξ=0.002 s^{-1}). As an example, an "apparent strain – apparent stress" diagram of the TNT (P=0.45) foam is shown in Fig. 3a. The following metrics are extracted from such diagrams: the apparent yield stress (σ_y*) and the apparent Young's modulus at ε = 0.2 (E*). The Young's modulus is determined for the 10th testing cycle from the tangent to the point of the maximum stress on the unloading portion of the stress-strain diagram, and the yield stress σ_y* corresponds to the intersection of the tangent lines with the elastic and the plateau regions.

2.4. Morphology versus mechanical properties

As an example, the evolutions of the TNZ foams' pore size (D50), apparent Young's modulus (E*) and yield stress (σ_y*) are plotted in Fig. 3b as functions of the foam porosity. For the pore size ranging from 100 to 600 µm (the general recommendation for porous metallic scaffolds [10]), the foam porosity varies from 0.35 to 0.45, the Young's modulus decreases from 13 to 8 GPa and the yield stress, from 260 to 130 MPa. This range of stiffness matches that of cortical bone, whereas this range of mechanical resistance comfortably exceeds that of human bone. Note that the resulted stiffness is still higher than that of trabecular bone (the main target of this study). In this respect, an appropriate post-sintering thermal treatment of metastable titanium alloys, such as the TNT and TNZ of

this study, offers an extra capacity to lower the foams' stiffness without altering their morphology, by creating conditions for triggering reversible α"→β martensitic transformation during mechanical loading [11].

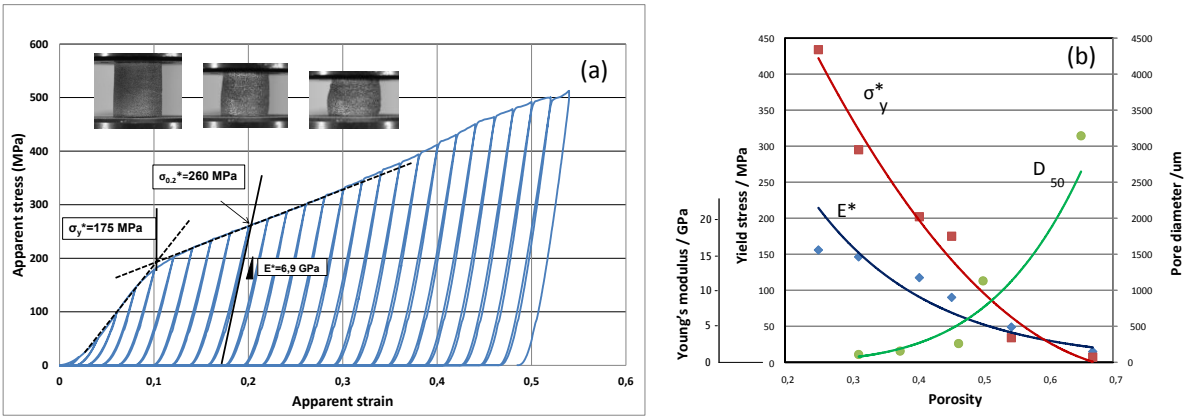

Fig. 3. (a) TNZ foam (P=0.45) compression test; (b) TNZ foams: pore size, apparent Young's modulus and yield stress as functions of porosity.

3. Modeling

Weighting the calculation power of modern desktop computers versus the structural complexity of real porous structures, the latter cannot be explicitly simulated by a single model ranging from a crystal lattice (Å) to an entire object (cm). Generally, a three-level modeling approach is applied: a micro-scale model simulating the behavior of the constitutive material, a macro-scale model simulating that of an entire object, and a meso-scale model bridging the gap between the micro- and the macro-models by explicitly representing the foam's architecture. Generally speaking, the larger the size of the meso-scale model, the more representative it is of the whole object, but the greater the computation time. The main challenge is therefore to determine the smallest size of the meso-scale model (representative volume element or RVE), while adequately representing the structural complexity of the object.

Since metallic foams should simultaneously satisfy functional requirements of the morphological and mechanical compatibility, both aspects should be considered when selecting the size of an RVE. To solve this problem, a numerical study should be performed to evaluate the dependence of the morphological and mechanical characteristics of the meso-scale model on its size (a convergence study).

To ensure the "mechanical" fidelity of the meso-scale model, the convergence of two characteristics can be analyzed: that of the stress-strain diagram σ=f(ε) and that of the strain distribution at different deformation stages φ(ε). To ensure the "morphological" fidelity of the meso-scale model, two other characteristics can be selected: the pore size distribution φ(D) and the specific surface area. Finally, the minimum size of a meso-scale model capable of simultaneously satisfying the criteria for morphological and behavioral fidelity can be determined, using the principle of a so-called "dominant constraint". The morphology-related numerical modeling of such foams is discussed in more detail in [12], whereas this communication is limited to the issue of "mechanical" convergence.

3.1. Foam generation

In this work, an original numerical generation algorithm is applied, capable of generating random foam structures with targeted porosities. These structures are composed of interconnected matter and interconnected void voxels, as shown in Fig. 4.

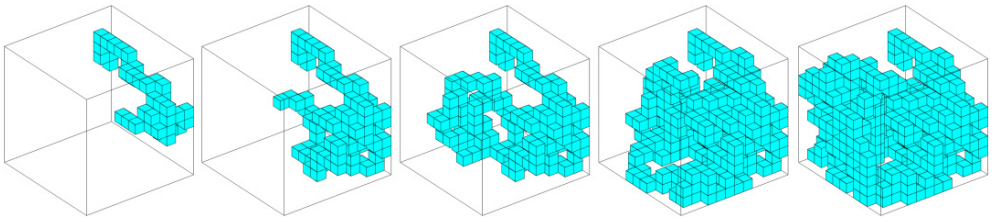

Fig. 4. Evolution of the path of matter Voxels (RVE = 12^3 and P=0.75) [12].

3.2. Mechanical convergence study

As a first approximation, mechanical convergence was studied using the phenomenological elastoplastic material law (Fig. 5a) and Von-Mises failure criteria in the ANSYS FEA software environment. The convergence study consisted of a series of displacement-controlled finite element simulations of a cubic domain with incrementally increasing RVE size (Fig. 5b); with the converged size of the domain leading to the stabilization of some selected metrics (Fig. 5e). In our case, the RVE size was increased from 4^3 to 80^3 by steps of 2^3, and the convergence metrics were E* (apparent Young's modulus), σ^*_y (apparent yield stress), and σ^*_u (apparent ultimate tensile strength). Note that each matter voxel corresponded to a single 20-node cubic finite element (FE). Convergence was considered to be reached when the deviation between six consecutive smoothed values of the selected metrics became less than 0.1%.

Since after each loading step, any matter element (voxel) could only be in one of the following states: elastically deformed, plastically deformed or failed, the corresponding volume fractions were calculated after each increment. Fig. 5c illustrates the evolution of these volume fractions superposed on the stress-strain diagram of RVE=50^3; this last value is considered to be converged for all of the metrics (Fig. 5d,e).

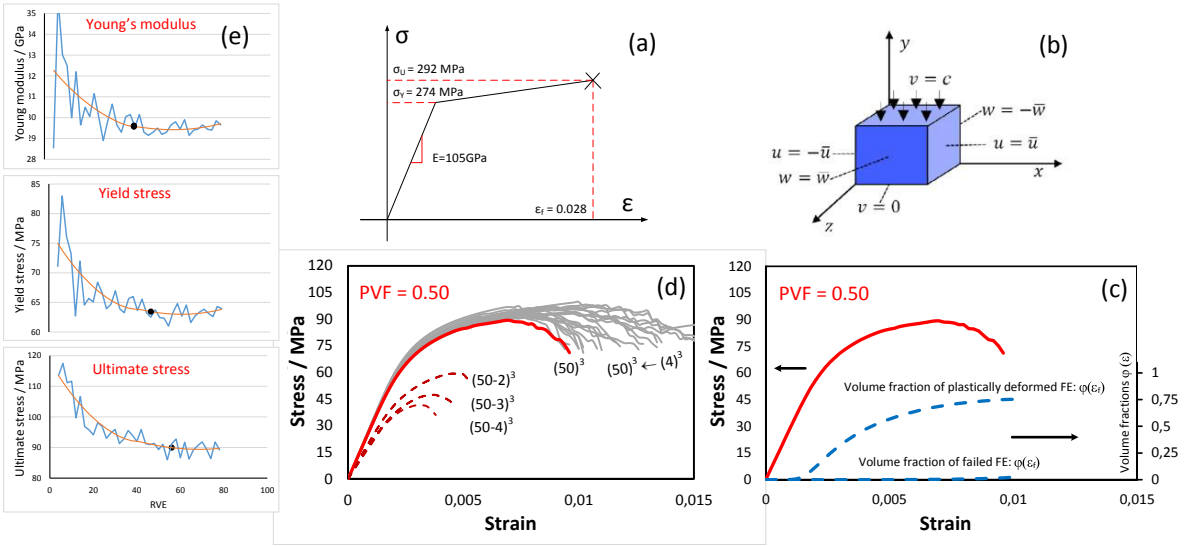

Fig. 5. (a) Elastoplastic material law; b) cubic domain and boundary conditions [12]; c) stress-strain diagram and evolution of volume fractions of the plastically deformed and failed elements, d) stress-strain diagram convergence: 1 voxel = 1 FE (4^3→50^3) and 1 voxel = 2, 3 and 4 FE [50-2, 50-3, and 50-4]^3; and e) Stress-strain diagram metrics convergence study (dots correspond to the convergent RVE for each metric).

4. Experiment versus modeling

For the as-sintered Ti-Cp, TNT and TNZ foams of this study, the Young's modulus and the yield stress values (experimentally measured and numerically calculated) are superposed in Fig. 6a,b. It can be observed that the calculated results are systematically higher than those obtained experimentally. This problem seems to be related to a non-sufficient refinement of the finite element model used for these calculations (1 voxel = 1 FE). The preliminary results obtained with 2^3, 3^3 and 4^3 FE per voxel show that the 1 voxel = 1 FE meso-scale model was not really representative (see Fig. 5d). This study is part of an ongoing project.

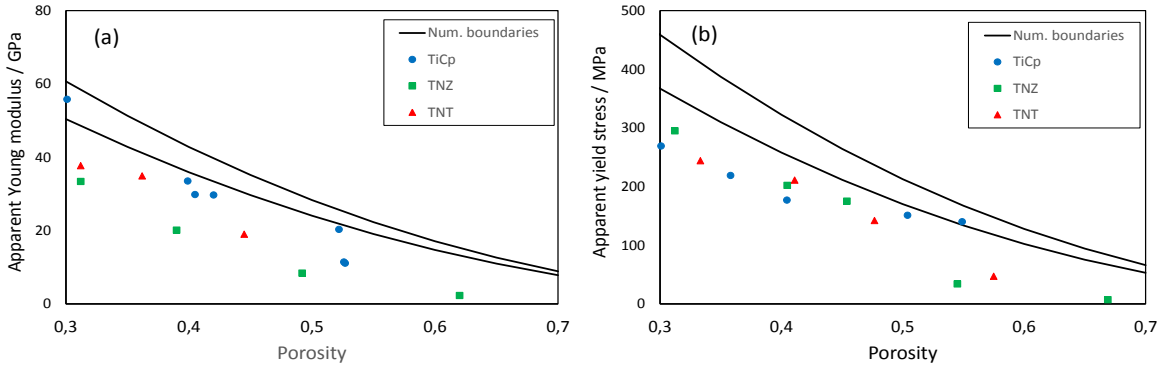

Fig. 6. Young's modulus (a) and yield stress (b) of the as-sintered Ti-Cp, TNT and TNZ foams of variable porosities (numerical versus experimental results).

Summary

1. The space-holder method enables TiCp, TNZ and TNT foams to be produced consistently in the 0.25 -- 0.65 porosity range with controlled microstructure, morphology and mechanical properties.
2. The representative volume element (RVE) approach appears to be capable of simultaneously satisfying the criteria for morphological and behavioral fidelity, at least for elastoplasticity and failure.

Acknowledgements

This work was supported by the *Fonds de recherche du Québec – Nature et technologies (FQR-NT)*, by the National Science and Engineering Research Council of Canada (NSERC), and by the Ministry of Education and Science of the Russian Federation: the Increase Competitiveness Program of NUST "MISiS" (K3-2014-017).

References

[1] R. Brånemark, P.I Brånemark, B. Rydevik, R.R. Myers, J. of Rehab. Res. and Dev. 38 (2001) 175–181.
[2] A. Fukuda, M. Takemoto, T. Saito, S. Fujibayashi, M. Neo, D.K. Pattanayak, T. Matsushita, K. Sasaki, N. Nishida, T. Kokubo, T. Nakamura, Acta Biomat. 7 (2011) 2327–2336.
[3] X. Liu, S. Wu, K.W.K. Yeung, Y.L. Chan, T. Hu, Z. Xu, X. Liu, J. C.Y. Chung, K.M.C. Cheung, P.K. Chu, Biomaterials 32 (2011) 330–338.
[4] S. Miyazaki, H.Y. Kim, H. Hosoda, Mater. Sci. Eng. A 438-440 (2006) 18–24.
[5] M. Arciniegas, J.M. Manero, J. Peña, F.J. Gil, J.A. Planell, Metal. Mater. Trans. A 39 (2008) 742–751.
[6] C.A. Simmons, S.A. Meguid, R.M. Pillar, J. Biomed. Mater. Res. 55 (2001) 63–71.
[7] A.E. Markaki, T.W. Clyne, Biomaterials 25 (2004) 4805–4815.
[8] G. Ryan, A. Pandit, D.P. Apatsidis, Biomaterials 27 (2006) 2651–2670.
[9] J. Rivard, V. Brailovski, S. Dubinskiy, Mater. Sci. Eng. C 45 (2014) 421–433.
[10] JD. Bobyn, J. Miller, In: Simon S. Ed. Orthopaedic basic science, Chicago, Amer. Acad. Orthopaedic Surgeons, 1994.
[11] V. Brailovski, S. Prokoshkin, M. Gauthier, K. Inaekyan, S. Dubinsky, J. Alloys. Comp. 577-1 (2013) 413–417.
[12] C. Simoneau, P. Terriault, J. Rivard, V. Brailovski, J. Comp. Mater. Sci. 51 (2014) 3633–3641.